Materials Science & Engineering A 713 (2018) 161–173

Contents lists available at ScienceDirect

Materials Science & Engineering A

journal homepage: www.elsevier.com/locate/msea

On the origin of the superior long-term creep resistance of a 10% Cr steel

R. Mishnev*, N. Dudova, R. Kaibyshev

Belgorod State University, Belgorod 308015, Russia

ARTICLE INFO

Keywords:
Martensite
Steel
Creep
Electron microscopy
Precipitation
Coarsening

ABSTRACT

A low-nitrogen 10% Cr martensitic steel containing 3% Co and 0.008% B was shown to exhibit an extremely long creep rupture time of $\sim 4 \cdot 10^4$ h under an applied stress of 120 MPa at 650 °C. The creep behavior and evolution of lath martensite structure and precipitates during creep at these conditions were studied. The main feature of the microstructure under long-term creep is retention of the lath structure until rupture. The following microstructural factors affecting the superior creep resistance were analyzed: (1) alloying by (W + Mo) elements; (2) particles of $M_{23}C_6$ and Laves phases; (3) homogeneously distributed M(C,N) carbonitrides. It was revealed that nanoscale $M_{23}C_6$ carbides and M(C,N) carbonitrides compensated the negative effects of W depletion from the solid solution and extensive coarsening of the Laves phase particles. $M_{23}C_6$ carbides demonstrate a high coarsening resistance under creep conditions and exert a high Zener drag pressure before rupture because of the coherency of their interfaces. The strain-induced transformation of a portion of the precipitated V-rich M(C,N) carbonitrides to the Z-phase does not affect the creep strength because the Z-phase particles are nanoscale and negligible in quantity.

1. Introduction

Creep-resistant martensitic steels with 9–11% Cr are favorable materials for the turbine components of fossil-fuel power plants [1,2]. Their alloying design and heat treatment aim to provide stability to the tempered martensite lath structure (TMLS), which comprises prior austenite grains (PAGs), packets, blocks, and laths with a high dislocation density in the lath interiors under creep conditions [1–3]. The dispersion strengthening in high-chromium steels is provided, mainly, by nanoscale boundary $M_{23}C_6$ carbides and homogeneously distributed in the lath interiors fine M(C,N)-type particles (where M is Nb and V).

The TMLS is the main factor in the superior creep strength of these steels during long-term creep [3–12]. Instability of TMLS under creep reduces the creep strength and yields to the creep strength breakdown. The long-term rupture time suddenly drops with increasing rupture time, thereby diminishing the creep strength at high rupture times [7–12]. However, the origin and nature of creep strength breakdown has not yet been elucidated [6–9,11].

Two processes promote the onset of creep strength breakdown: a knitting reaction and subgrain coarsening. The knitting reaction occurs between the gliding dislocations and lath boundaries; this leads to transformation of the lath dislocation boundaries, which are irregular dislocation networks that exert long-range stress fields, to sub-boundaries, thereby relieving the internal stress fields [4,10–13]. The knitting reaction annihilates the lattice dislocations and dislocations that comprise the interlath boundaries [4,10–13]. This process requires dislocation climb and is the kinetic process that is responsible for transient creep in high-Cr steels [4]. It is worth noting that a slip on the $\{110\}_\alpha$ plane with two possible $< 111 >_\alpha$ slip directions intrinsically proceeds parallel to the lath boundaries [14,15]. The dislocation glide along the laths occurs very slowly because the gliding dislocations are connected to the lath boundaries, which act as effective pinning agents [13,14]. In addition, the boundary $M_{23}C_6$ carbides/Laves phase particles and M(C,N) carbonitrides that are homogeneously distributed within the lath interiors [1,2,10–12] effectively pin the gliding dislocations, providing significant dispersion hardening [13,14]. Only a minor portion of the lattice dislocations can glide across a lath; therefore, lath boundaries act as dislocation sources. The dislocations generated by the lath boundaries glide inside the lath until they encounter another lath boundary [13,14]. Only the M(C,N) carbonitrides pin such gliding dislocations [13]. The transformation of V-rich M(C,N) carbonitrides to coarse Z-phase particles (CrVN), which is the form of the nitride in thermodynamic equilibrium, is proposed to cause creep strength breakdown [16–18]. Substitutional atoms such as W, Mo, and Co also hinder the knitting reaction and provide solid solution hardening [1,19,20]. In addition, these solutes impede diffusion, thereby slowing the rearrangement of lattice dislocations by climb, which also hinders the knitting reaction [11,13,14,19,21].

The second process, subgrain coarsening, significantly decreases the lattice dislocation density [3,4,7,8,11,19–25]; this is attributed to a

* Corresponding author.
E-mail address: mishnev@bsu.edu.ru (R. Mishnev).

https://doi.org/10.1016/j.msea.2017.12.066
Received 30 August 2017; Received in revised form 13 December 2017; Accepted 14 December 2017
Available online 15 December 2017
0921-5093/

decrease in the pinning pressures that originate from boundary $M_{23}C_6$ carbides due to strain-induced coarsening of these particles; this mainly occurs below the critical interval of 0.08–0.12 MPa [11,12,19,21–24]. Thus, the alloying philosophy for increasing the creep strength of 9–11% Cr steel includes the formation of dispersions of secondary phase particles, which suppress or hinder the knitting reaction by pinning the lattice dislocations, and transformation of the TMLS to a subgrain structure by exerting a high Zener drag force [10–13,19–26].

This approach was used to develop a new generation of 9–10% Cr steels that do not exhibit creep strength breakdown up to an extremely long rupture time of $\sim 4{\cdot}10^4$ h owing to high B and low N contents [12,27–32]. The high B content separates the dispersion of boundary $M_{23}C_6$ carbides into two phases: B-free $M_{23}C_6$ carbides and $M_{23}(B{\cdot}C)_6$ [33,34]. The $M_{23}(B{\cdot}C)_6$ phase is much more resistant to coarsening than the B-free $M_{23}C_6$ carbides because of the decreased energy of the $Fe_\alpha(110)||M_{23}(B{\cdot}C)_6(111)$ interfaces [12,32,33,35], in accordance with the well-known Gibbs–Thomson scheme [36]. In addition, the lower N content prevents the formation of BN and significantly reduces the volume fraction of V- and N-rich M(C,N) particles, which may transform into coarse Z-phase particles [1,12,34,37,38]. It is known that the separation of M(C,N) carbonitrides into two phases comprising Nb-rich carbonitrides enriched with C and V-rich particles enriched with N increases the resistance of these dispersoids to coarsening and is responsible for the superior creep resistance of 9–11% Cr steels [1,2,11,19,22–24,39]. The low-volume fraction of V-rich carbonitrides precipitates during tempering in 9–10% Cr steels with low N contents [34,37,38]. However, the role of V in the precipitation behavior is yet to be elucidated [12].

It has been reported that the TMLS of a 10% Cr steel with 3% Co, 0.008% B, and 0.003% N remains very stable under short-term creep; this was attributed to the low susceptibility of boundary $M_{23}C_6$ carbides to coarsening [12]. Although the applied stress was sufficiently high (140 MPa), the knitting reaction under transient creep was very slow and the pinning pressure imparted by the $M_{23}C_6$ carbides was sufficient to suppress the replacement of TMLS with a subgrain structure. However, the role of microstructural changes in the long-term creep behavior and superior creep resistance without creep strength breakdown up to an extremely long rupture time for these 10%Cr steels has not been investigated in sufficient detail. The aim of the present work is to elucidate the origin of the elimination of creep strength breakdown up to $4{\cdot}10^4$ h at 650 °C under long-term creep with an applied stress of 120 MPa in this steel. Specific attention will be paid to the effect of the dispersion of the secondary phases on the stability of TMLS.

2. Experimental procedure

A 10% Cr steel with the following chemical composition (in mass%) of 0.1% C; 0.06% Si; 0.1% Mn; 10.0% Cr; 0.17% Ni; 0.7% Mo; 0.05% Nb; 0.2% V; 0.003% N; 0.008% B; 2.0% W; 3.0% Co; 0.002% Ti; 0.006% Cu; 0.01% Al and Fe balance was solution treated at 1060 °C for 0.5 h, cooled in air, and subsequently tempered at 770 °C for 3 h. Other details for material preparation were reported previously [12,29,34,37]. Flat specimens with a gauge length of 25 mm and cross-sectional dimensions of 7 mm × 3 mm were crept to various strains by interrupting creep and until rupture at an applied stress of 120 MPa and a temperature of 650 °C.

The evolution of microstructure and the dispersion of secondary phase particles were examined under conditions of long-term aging in grip sections and creep in gauge lengths. Structural characterization was performed using a Jeol JEM-2100 transmission electron microscope (TEM) with an INCA energy dispersive X-ray spectrometer and using the Z-contrast technique with a Quanta 600FEG scanning electron microscope (SEM) equipped with an electron backscatter diffraction (EBSD) pattern analyzer incorporating an orientation imaging microscopy (OIM) system. Low and high angle boundaries (LABs and HABs) were defined to have a misorientation of $2^\circ < \theta \leq 15^\circ$ and $> 15^\circ$ and depicted in misorientation maps using white and black lines, respectively. In order to evaluate the distribution of strain or the stored energy in TMLS the Kernel average misorientation (KAM) values were calculated [15,40]. The KAM value for each pixel is defined as the average misorientation that a pixel has with six neighbors [39]. The transverse lath/subgrain sizes were measured on the TEM micrographs by the linear intercept method, counting all the clear visible (sub)boundaries [11–13,19,21–23]. The dislocation densities were estimated by counting the individual dislocations in the (sub)grain/lath interiors per unit area on at least six arbitrarily selected typical TEM images for each data point [11–13,19,21–23,35]. The density of particles located at (sub)grain/interlath boundaries was determined as the number of particles per unit boundary length [11,12,19]. Identification of the precipitates in TEM investigations was performed based on a combination of EDS composition measurements of the metallic elements and indexing of electron diffraction patterns [11,12,35,38,39]. Dimensions of secondary phase particles were calculated using replica technique described in previous works [11,12,19,21–23,35,38,39] in full details.

The equilibrium volume and mole fractions of phases and their chemical compositions were calculated by the version 5 of the Thermo-Calc software using the TCFE7 database by entering the BCC A2, FCC A1, M23C6 and LAVES PHASE C14 as equilibrium phases for the actual steel composition [11,38,39]. To estimate the coarsening of the $M_{23}C_6$ and Laves phase particles the calculation was performed by the TC-Prisma software using the kinetic MOBFE1 and thermodynamic TCFE6 databases [21] for the composition of (in mass%): 0.1% C; 10% Cr; 3.1% Co; 0.7%; Mo; 2.0% W and Fe balance.

3. Results

3.1. Tempered martensite lath structure

The microstructure and distribution of secondary-phase particles in the 10% Cr steel after heat treatment were described in previous works [12,29,34,37,41] in details and summarized in Table 1. The meso-scale strain distribution indicated by the KAM map (Fig. 1(a)) [15] is non-uniform. Highly misoriented areas of fine laths alternate with low-misoriented coarse laths within packets. Almost no LABs with a

Table 1
Evolution of structural parameters of the 10% Cr steel during creep testing at 650 °C under a stress of 120 MPa.

Structural parameters		Initial state	Gauge / grip	Gauge / grip	Gauge / grip	Creep ruptured gauge / grip
Time, h		0	1000	10000	28286	39437
Lath width, nm		380	423 / 409	552 / 507	695 / 566	861 / 614
Dislocation density, $\times 10^{14}$ m^{-2}		1.7	0.75 / 1.23	0.51 / 1.06	0.43 /0.61	0.20 / 0.43
Mean size of particles, nm	$M_{23}C_6$	70	73.9 / 72	84.6 / 81.9	115.2 / 83.6	120.4 / 96
	Laves phase	—	147.1 / 145.6	221.9 / 197.6	334.2 / 298.81	373.7 / 319
	Nb-rich MX	30	35.7 / 35	36.3 / 31.3	37.6 / 31.6	38.5 / 35
	V-rich MX	40	— / —	60.7 / 26.5	65.6 / 40	67.09 / 58
	M_6C	25	— / —	— / —	— / —	— / —
	Z-phase	—	— / —	— / —	— / —	120 / —

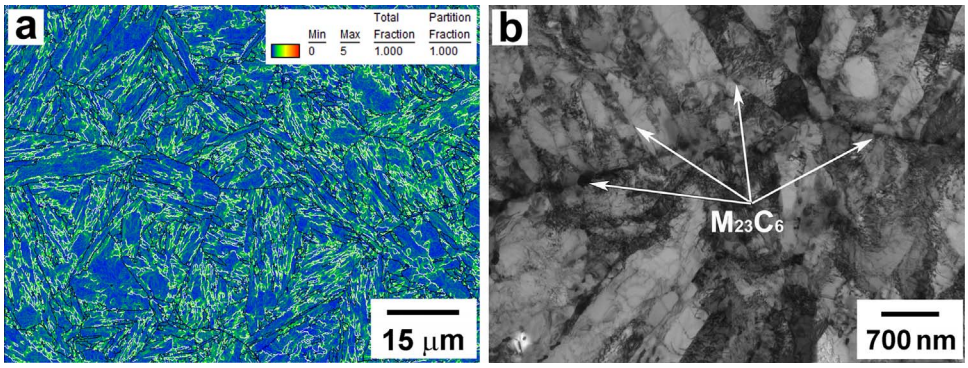

Fig. 1. Microstructure of the 10% Cr steel after heat treatment: (a) the KAM map (a) and SEM micrograph (b).

misorientation > 2° were observed within the coarse laths, which comprise ~35% of the laths. Therefore, the strain is predominantly localized in blocks, whereas coarse laths are almost strain-free [42]. It is worth noting that the density of geometrically necessary dislocations is associated with the KAM value [43]. Both structural components have similar lattice dislocation densities, as calculated by TEM [12,37].

The precipitation structure consists of $M_{23}C_6$ carbides with an average size of about 70 nm located at HABs of PAGs, packets, and blocks and LABs of laths nearly in the equal proportion (Fig. 1(b)). Nb-enriched M(C,N) carbonitrides with sizes of 30 nm are uniformly distributed within the martensite laths. It should be noted that V-rich M(C,N) particles are rarely observed in tempered 10% Cr steel and comprise approximately 1% of all particles of all types of replicas analyzed by TEM (only 5 particles were identified as V-rich carbonitrides among ~500 analyzed particles). Scarce, fine W-rich M_6C carbides with an average dimension of 25 nm were found whereas no Laves phase precipitates were observed.

3.2. Creep behavior

The rupture time of 10% Cr steel is linearly dependent on the applied stress (Fig. 2(a)). In contrast to P92 steel, creep strength breakdown was not observed up to a rupture time of 39437 h. The $\dot{\varepsilon}$ vs. t and $\dot{\varepsilon}$ vs. ε curves at 120 MPa are shown in Fig. 2(b) and (c), respectively. The transient creep strain, ε_T, the duration of apparent steady-state creep ($\dot{\varepsilon}_{min}\cdot t_r$, where t_r is the rupture time) and tertiary creep strain, ε_3, values were calculated (Fig. 2(c)) using the technique described in literature [12,44,45]. Under transient creep, the decrease in the creep rate with time is characterized by the rate of exhaustion of transient creep, i.e., $r' = 1.94\cdot10^{-4}\ h^{-1}$, as evaluated using the following relationship, which was proposed by Garofalo [44,45]:

$$\varepsilon = \varepsilon_0 + \varepsilon_T[1 - \exp(-r'\cdot t)] + \dot{\varepsilon}_s\cdot t, \quad (1)$$

where ε is the strain, ε_0 is the instantaneous strain on loading, $\dot{\varepsilon}_s$ is the steady-state creep rate, which can be replaced by the $\dot{\varepsilon}_{min}$ value [45], and t is the time. r' was evaluated graphically as the slope of the plot of $\ln(1 - \Delta/\varepsilon_T)$ vs. time, where Δ is the transient creep component ($\Delta = \varepsilon - \varepsilon_0 - \dot{\varepsilon}_{min}\cdot t_r$) [45]. The creep rate decreases by a factor of $\sim10^4$ under transient creep. Reducing the applied stress from 140 to 120 MPa decreases the magnitude of the strain rate drop by a factor of ~25 from the refined value at 140 MPa ($r' = 5\cdot10^{-3}\ h^{-1}$ [12]) and the ε_T value from 2.2% to 1.58% (Fig. 2(c), Table 2). On the other hand, the decrease in the creep rate with strain at the transient stage is characterized by a $d\ln\dot{\varepsilon}/d\varepsilon$ of ~ −576, which is consistent with $\dot{\varepsilon}\sim A\exp(b\varepsilon)$ [9]. The absolute value of this parameter is ~4 times higher than that at 140 MPa [12]. Therefore, reducing the applied stress from 140 to 120 MPa strongly promotes the reaction-rate kinetics during transient creep [45].

At 120 MPa, the 10% Cr steel exhibits a minimum creep rate, $\dot{\varepsilon}_{min}$, instead of steady state that is typical for martensitic steels [1]. The minimum creep rate is attained at a strain of 2.5% instead of 3.5% and

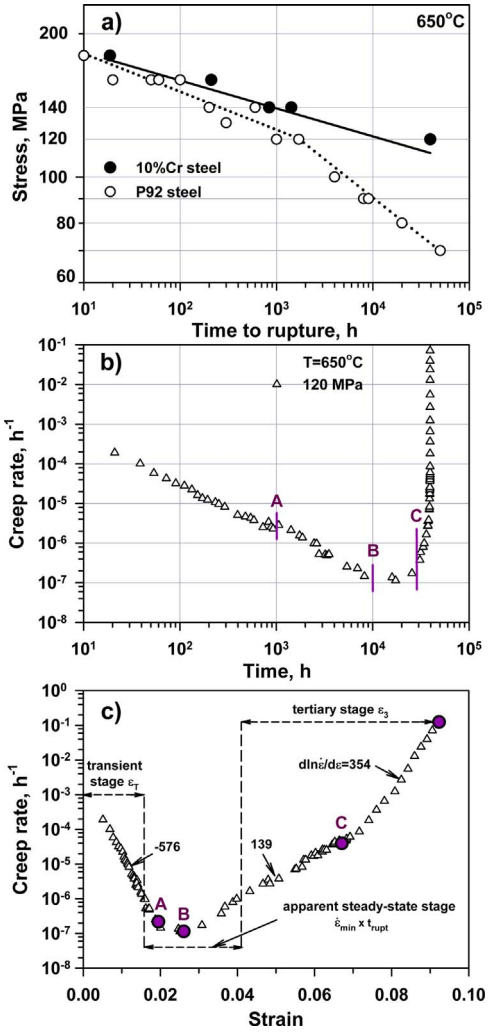

Fig. 2. Time to rupture *vs* stress curve (a) and creep rate *vs* time (b) and strain (c) curves at 120 MPa (b) of the 10% Cr steel at 650 °C. Data for P92 steel is taken for comparison from [12].

is $\sim1.15\cdot10^{-7}\ h^{-1}$, which is approximately two orders of magnitude lower than that at 140 MPa [12]. Nevertheless, the apparent region of steady-state creep, i.e., $\dot{\varepsilon}_{min}\cdot t_r$ [46] (Fig. 2(c)), is nearly the same (2.52%) as that at 140 MPa (3.14%) as the duration is ~25 times longer [12].

Two stages of tertiary creep [11] could be distinguished in the slope of the creep curve (Fig. 2(c)). In the first stage, which involves low acceleration of the creep rate, $d\ln\dot{\varepsilon}/d\varepsilon$ (~139) is approximately 1.5 times higher than that at 140 MPa [12]. During the second stage, which comprises rapid acceleration of the creep rate, the $d\ln\dot{\varepsilon}/d\varepsilon$ value is

Table 2
Parameters of creep behavior of the 10% Cr steel during creep testing at 650 °C under a stress of 120 MPa in comparison with data at 140 MPa [12].

Applied stress, MPa	$\dot{\varepsilon}_{min}$, h^{-1}	t_r, h	ε_{min}, %	ε_T, %	$\dot{\varepsilon}_{min} \cdot t_r$, %	ε_3, %	r', h^{-1}	p, h^{-1}
120	$1.15 \cdot 10^{-7}$	39437	2.51	1.58	2.52	5.2	0.000194	0.000151
140	$1.4 \cdot 10^{-5}$	1426	3.5	2.19	3.14	10.55	0.005	0.01

~354. The extent of the tertiary creep stage is 5.2%, which is half that at 140 MPa [12] (Table 2). The elongation-to-failure under creep decreases from ~16% to ~9% upon decreasing the applied stress from 140 [12] to 120 MPa. The rate of acceleration of tertiary creep with time, p, was evaluated as follows [46]:

$$\varepsilon = \varepsilon_0 + \varepsilon_T[1 - \exp(-r' \cdot t)] + \dot{\varepsilon}_s \cdot t + \varepsilon_3 \exp[p(t - t_r)], \quad (2)$$

where ε_3 is the tertiary creep strain; this value was obtained graphically from the slope of the plot of $\ln(\Delta/\varepsilon_3)$ vs. $(t - t_t)$, where Δ is the tertiary creep component ($\Delta = \varepsilon - \varepsilon_0 - \varepsilon_T - \dot{\varepsilon}_{min} \cdot t_r$) and t_t is the time to onset of the tertiary stage ($1.5 \cdot 10^{-4}$ h^{-1}) (Table 2). The p value at 120 MPa is significantly lower than that at 140 MPa [12]. Therefore, at 120 MPa, the recovery processes occur at low rates under tertiary creep, and the high $d \ln \dot{\varepsilon}/d\varepsilon$ values are indicative of the relatively complete recovery related to decreased strain. Thus, analysis of the creep curves showed that the transition from 140 to 120 MPa strongly promotes the kinetic process under transient and tertiary creep.

3.3. Microhardness

Fig. 3(a) shows the change in the microhardness of tested specimens in the grip and gauge sections. Long-term aging and long-term creep result in the 5% and 14% decrease in microhardness, respectively.

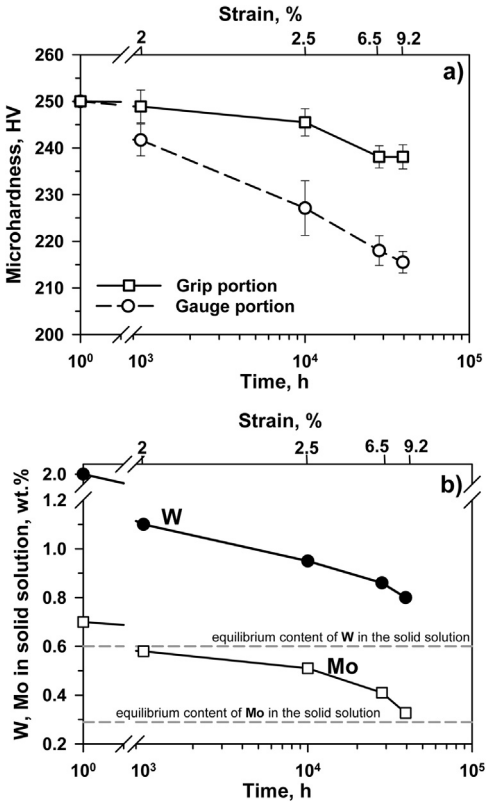

Fig. 3. (a) Change in microhardness during creep testing at 650 °C under a stress of 120 MPa in the grip and gauge portions of the 10% Cr steel. (b) Change in the W and Mo contents in the solid solution of the 10% Cr steel in the gauge portion of the specimens after creep tests at 650 °C under a stress of 120 MPa estimated from foils by EDX with TEM.

Transient creep led to a 9% decrease in the microhardness and further apparent steady-state provides a 4% additional decrease despite the fact that time durations for transition and steady-state creep are nearly the same. Decrease in microhardness under tertiary creep is insignificant.

3.4. TMLS during long-term aging and creep

The microstructural evolution of 10% Cr steel was examined using creep-interrupted specimens A, B, and C (Fig. 2(b) and (c)), which represent the onset of apparent steady-state creep before attaining the minimum creep rate (~10^3 h), offset creep rate (~10^4 h), and second stage of tertiary creep (28286 h), respectively, as well as after rupture (39437 h) under long-term aging in grip sections and long-term creep in gauge sections. During long-term aging at 650 °C, the changes in the lath thickness and dislocation density are insignificant up to 10^4 h; however, a 49% increase in lath thickness and approximately 3-fold decrease in lattice dislocation density occurs after 28286 h (Fig. 4(a) and (b), Fig. 5(a) and (b), Table 1). Further aging for 39437 h leads to insignificant changes in the structural parameters (Fig. 4(c)–(e), Table 1) with complete retainment of the TMLS. Neither the destruction of "Bain" circles [12,47] nor a decrease in the mean KAM value (~0.68°) were evident (Fig. 4(e) and (f)). Therefore, the results of long-term aging under applied stresses of 140 (1426 h) and 120 MPa (~$4 \cdot 10^4$ h) are distinguished by static lath coarsening. Increasing the aging duration by a factor of ~28 leads to a significant decrease in the lattice dislocation density. Long-term aging did not affect the ratio of low-misoriented coarse laths and highly misoriented blocks. The proportion of LABs with misorientations ≤4° increased by a factor of ~1.5 after $2.8 \cdot 10^2$ [12] and ~10^4 h of aging (Fig. 4(e)).

Under creep conditions at 650 °C, the lath structure was also retained until rupture (Fig. 6). "Bain" circles on the {001} pole figures are partially destroyed during tertiary creep, which provides evidence for slight re-orientation of the crystal lattice under creep [46]. No evidence of the formation of equiaxed subgrains [11,41] was found. A tendency for increasing the LAB fraction with a misorientation of 2° was evident during the transient and apparent steady-state stages of creep (Fig. 6(a) and (c)); in contrast, the fraction of LABs with a misorientation of ~6° increased during the tertiary creep stage (Fig. 6(e) and (g)). The density of LABs continuously decreased under creep loading (Fig. 7(a)), which was attributed to lath coarsening and significantly facilitated by creep (Fig. 5(a)). As a result, strain results in a greater decrease in lattice dislocation density than long-term aging (Fig. 5(b)).

After transient creep, the lath thickness is almost the same in the gauge and grip sections, whereas the dislocation density in the gauge sections is ~2 times lower than that in the grip sections (Table 1, Figs. 5(a) and (b), 8(a)); these results are similar to those for a P92 steel [13]. The knitting reaction is attributed to trapping of the lattice dislocations by lath boundaries followed by partial destruction of the extrinsic and intrinsic dislocations with opposite signs because the average misorientation of the lath boundaries and their density remain almost unchanged [13]. The high $d \ln \dot{\varepsilon}/d\varepsilon$ value of ~−576 (Fig. 2(c)) was attributed to the fast disappearance of mobile lattice dislocations [13]. The ratio of low-misoriented coarse lath and highly misoriented blocks with strain localization remained the same within the PAGs (Fig. 7(b)). However, no strain localization was found in the vicinity of some boundaries of the PAGs (Fig. 6(b)). Therefore, the significant relief of the internal stress under transient creep [13] was attributed to elimination of strain localization near the PAG boundaries. After

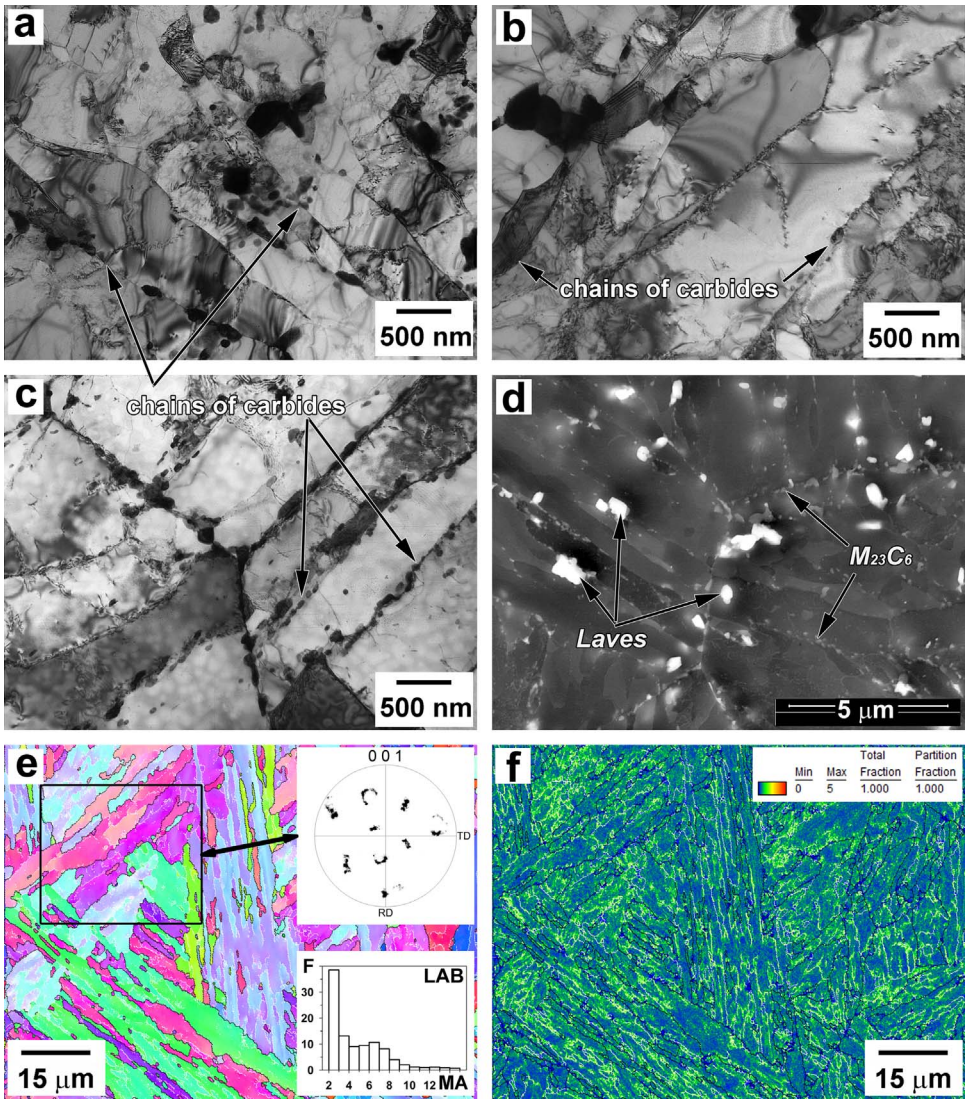

Fig. 4. Microstructure of the 10% Cr steel after long-term aging (in the grip portions of the specimens after creep tests at 650 °C under a stress of 120 MPa) for: (a) 10000 h, TEM micrograph; (b) 28286 h, TEM micrograph; (c) 39437 h, TEM micrograph; (d) 39437 h, SEM micrograph; (e) 39437 h, OIM image with {001} pole figure and distribution of LAB misorientation (F – fraction, (%), MA – misorientation angle, (degree)); (f) 39437 h, kernel average misorientation map.

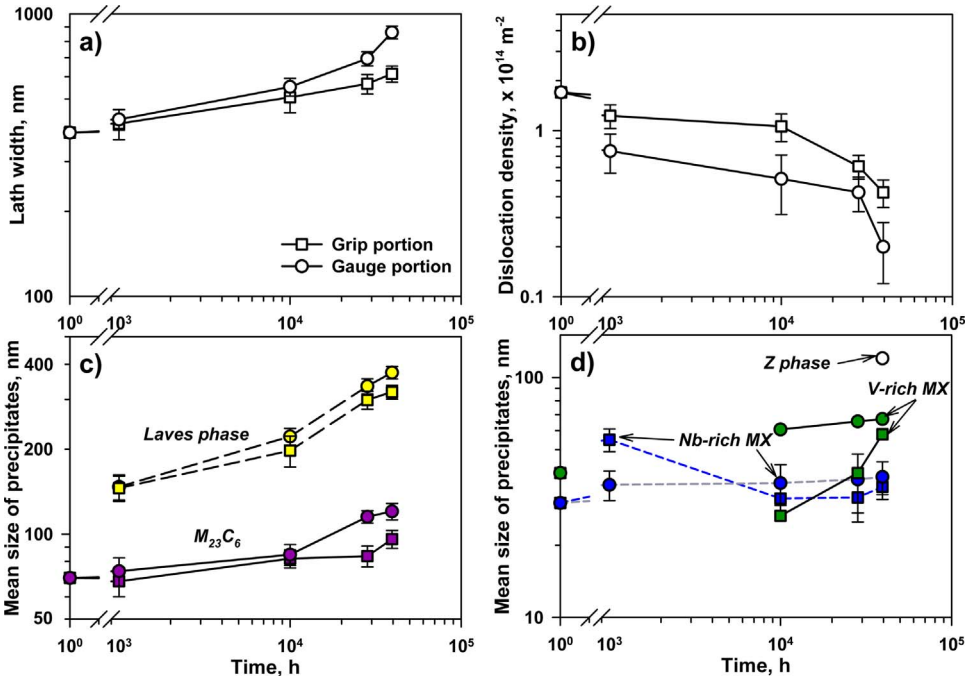

Fig. 5. Changes in the lath width (a), dislocation density (b) and in the mean size of precipitates (c, d) with time in the gauge and grip sections of the 10% Cr steel specimens during creep testing at 650 °C under a stress of 120 MPa estimated by TEM.

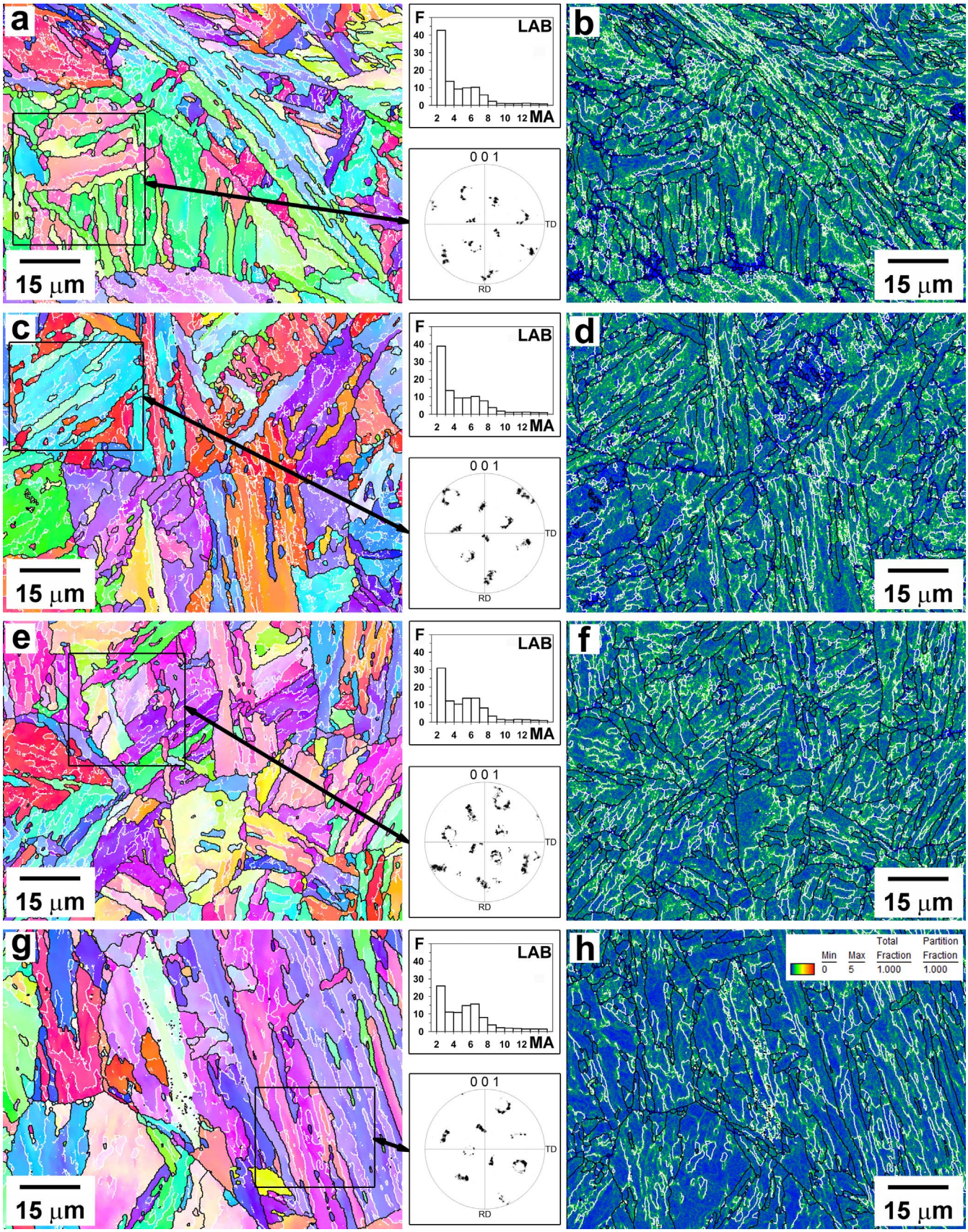

Fig. 6. OIM images with {001} pole figures and distributions of LAB misorientation (a, c,e,g) and the KAM maps (b, d,f,h) in the 10% Cr steel in the gauge section of specimens after creep testing at 650 °C under a stress of 120 MPa: (a, b) specimen A (1000 h); (c, d) specimen B (10000 h); (e, f) specimen C (28286 h); (g, h) ruptured specimen (39437 h).

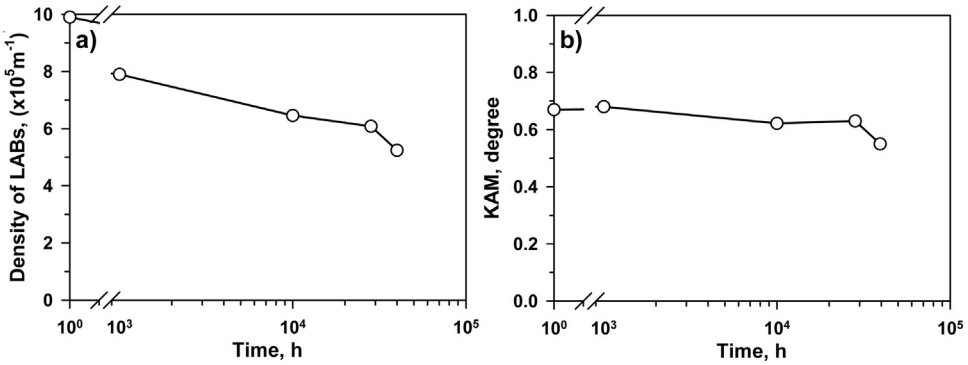

Fig. 7. Change in density of LABs (a) estimated on OIM images, and kernel average misorientation (b).

transient creep, the highly misoriented areas alternate with areas of uniform orientation along these boundaries.

The ratios of the lath thickness and dislocation density in the gauge and grip sections remained nearly the same under steady-state creep (Table 1. Fig. 5(a) and (b)). Lath coarsening is the main driver of microstructural evolution leading to the gradual decrease in the density of LABs (Fig. 7(a)). The number of low-misoriented coarse laths increases and continuous areas with no strain localization appear along the PAG boundaries (Fig. 6(d)). Some of the lath boundaries become thinner and exhibit extinction contours (Fig. 8(b)). New lattice dislocations result from the knitting out of lath boundaries [13]. This process is associated with rearrangement of intrinsic dislocations in lath boundaries that leads to the disappearance of some LABs. The knitting reactions do not significantly affect the dislocation density because the rates of emission and elimination of lattice dislocations with the same signs are nearly equivalent [13].

Remarkable strain-induced lath coarsening appears during the first stage of tertiary creep. This process was attributed to the transformation of some interlath boundaries to subgrain boundaries (Figs. 5(a) and 8(c), Table 1). It is worth noting that evidence for the occurrence of this process was found during long-term aging (Fig. 4(c) and (d)): Low-misoriented blocks appeared within the PAGs (Fig. 6(f)) because of the knitting reactions. The increasing lath thickness facilitates dislocation glide, thereby generating a high $d \ln \dot{\varepsilon}/d\varepsilon$ value of ~139 [13]. Gliding dislocations are effectively pinned by matrix carbonitrides, and the decrease in the lattice dislocation density is insignificant. During the secondary stage of tertiary creep, the strain-induced lath coarsening accelerates (Figs. 5(a) and 6(g) and (h), Table 1), which leads to a decrease in the lattice dislocation density to a typical value for long-term creep [11,13,21,22]. A significant portion of the LABs with misorientations < 4° disappear. Low-misoriented coarse laths containing no LABs become dominant, which leads to a remarkable decrease in the KAM average value (Fig. 7(b)). Therefore, at this stage, the density of geometrically necessary dislocations and overall dislocation density concurrently decrease. Retention of the lath structure was attributed to boundary $M_{23}C_6$ carbides and Laves phase particles, which effectively pin the interlath boundaries (Fig. 8(d)). Detachment of the interlath boundaries from the chains of boundary particles was rarely observed and only in the ruptured specimen.

3.5. Precipitate structure

W and Mo are depleted from the solid solution during long-term aging and creep (Fig. 3(b)); this depletion is accelerated by strain [21]. The majority of the thermodynamic non-equilibrium content of W and a minor portion of the Mo in ferrite are depleted under transient creep.

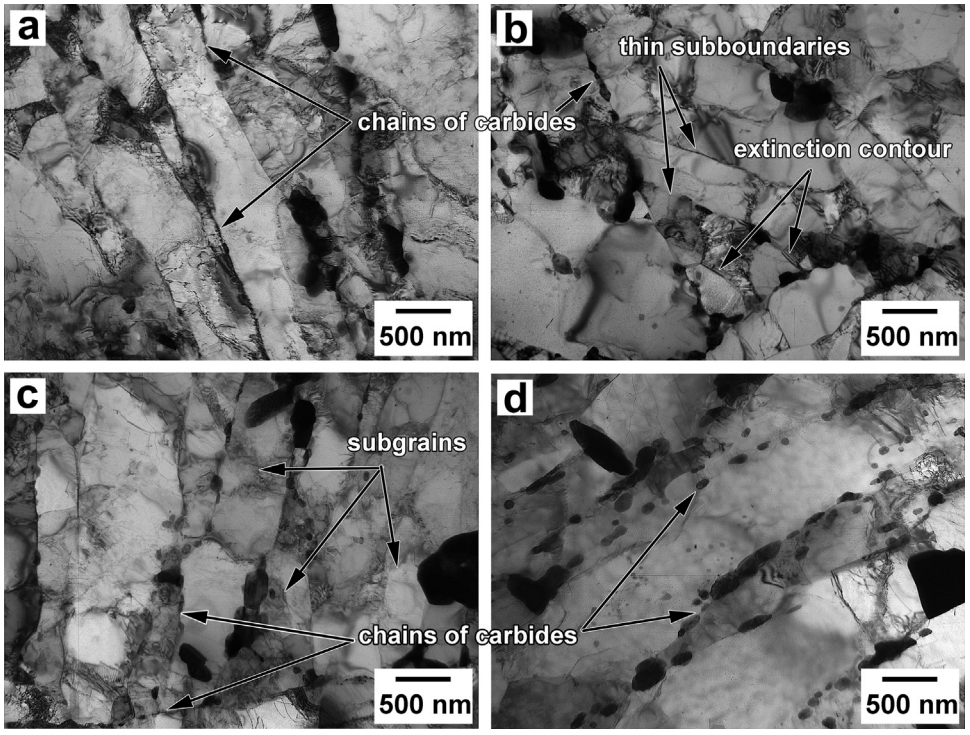

Fig. 8. TEM micrographs of the 10% Cr steel in the gauge section of specimens after creep tests at 650 °C under a stress of 120 MPa: (a) specimen A (1000 h); (b) specimen B (10000 h); (c) specimen C (28286 h); (d) ruptured specimen (39437 h).

Under steady-state creep, this depletion occurs at a low rate for both solutes. Under tertiary creep, the thermodynamic equilibrium content of Mo is attained while the content of W in the solid solution exceeds the thermodynamic equilibrium value even after $\sim 4{\cdot}10^4$ h.

During long-term aging ($\tau \leq 10^3$ h), the evolution of a dispersion of secondary-phase particles reported in previous work [12] and observed in the present study (Fig. 4, Table 1) is nearly the same. A distinct difference occurs in the precipitation of V-rich M(C,N) carbonitrides and the larger dimensions of the Laves phase particles at $\tau \geq 10^4$ h. The high-angle boundaries of the PAGs, packets, and blocks and low-angle interlath boundaries are decorated by fine and densely located $M_{23}C_6$ carbides and Laves phase particles (Fig. 4)). W-rich Laves phase particles are evident as bright white particles in the SEM images obtained using the Z-contrast technique [48]; in contrast, the $M_{23}C_6$ carbides appear as grey particles. The volume fraction of $M_{23}C_6$ carbides tends to slightly increase with increasing time up to 10^4 h. Static coarsening provides a 24% increase in their dimensions after $\sim 4{\cdot}10^4$ h. However, there is no evidence of dissolution of these carbides along the interlath boundaries accompanied by extensive coarsening of $M_{23}C_6$ carbides located at the HABs. These particles generate the chains along the interlath boundaries (Fig. 4(c)).

The majority of the Laves phase particles precipitate during the 10^3 h of long-term aging; this is accompanied by dissolution of M_6C carbide, which is a transition phase [34]. Further aging leads to an insignificant increase in the volume fraction of this phase. The onset of extensive coarsening of the Laves phase occurs after 10^4 h (Figs. 5(c) and 9(f)). However, in contrast with steels containing 0.1 wt% C and 0.05 wt% N [11,19,21,47,48], these particles are located at both HABs and lath boundaries (Fig. 4d), as seen in a 9% Cr steel with low C content [49]. Insignificant coarsening of the Nb-rich M(C,N) carbonitrides occurs (Fig. 5(d)). The main feature of the 10% Cr steel is precipitation of V-rich carbonitrides during long-term aging ($> 10^3$ h). It is known that this type of carbonitride is enriched by N [11,19,21–23,38]. However, the amount of nitrogen is negligible in the present steel; therefore, the V-rich carbonitride could only be enriched by C. Precipitation of such carbonitrides requires long-term aging ($\geq 10^4$ h), and they are susceptible to extensive coarsening upon further aging. This is not typical for M(C,N) carbonitrides in other 9–11% Cr steels [11,19,21–23,48,50,51]. No evidence for the formation of Z-phase [16–18] was found.

Under transient creep, no strain-induced precipitation or particle coarsening was evident (Table 1, Figs. 8(a), 9(a), 10(a)). Chains of $M_{23}C_6$ carbides and Laves phase particles appear along the majority of interlath boundaries. The precipitation structures in the grip and gauge length are almost the same. Steady-state creep strongly accelerates the precipitation and growth of V-rich M(C,N) carbonitrides within the ferritic matrix (Table 1, Fig. 10(b)). The dimensions of these dispersoids in the gauge length after termination of the steady-state stage and in the

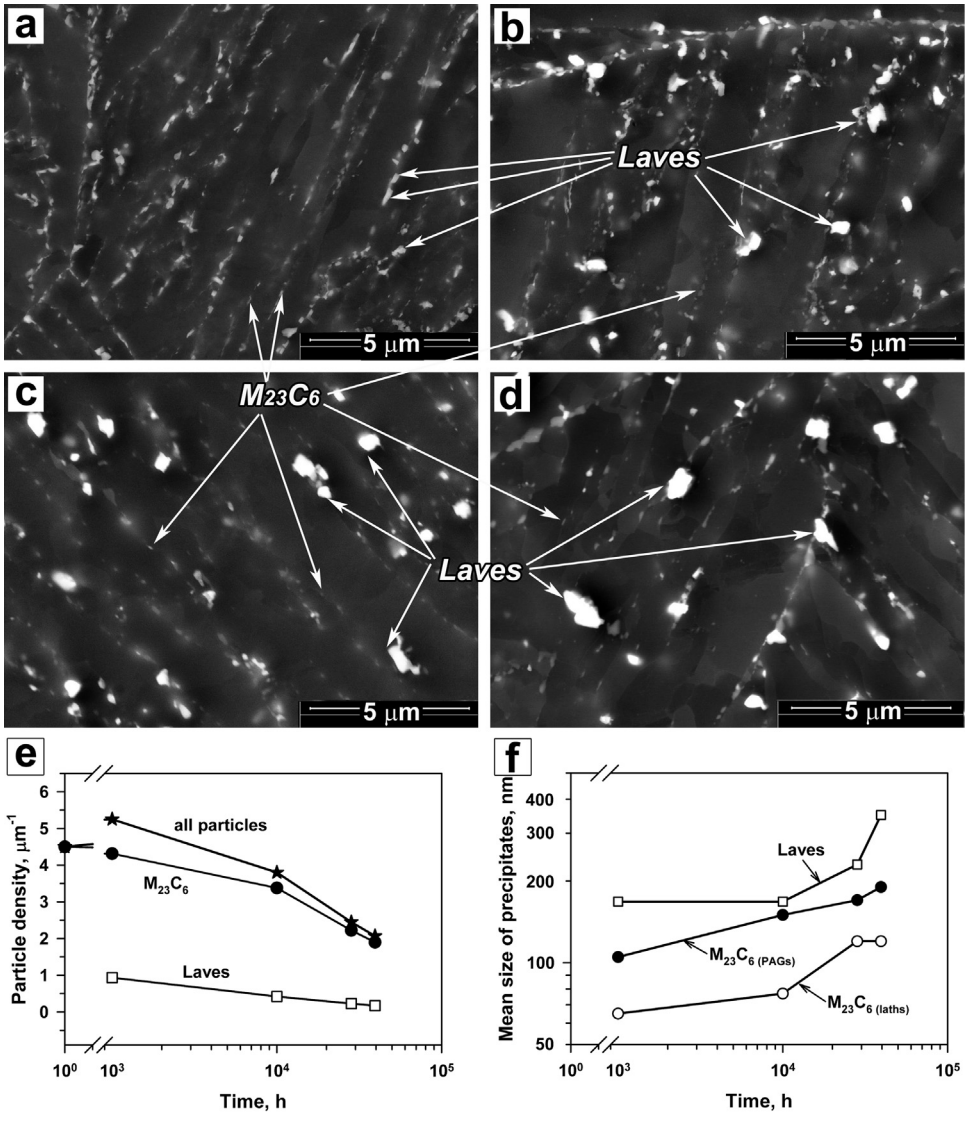

Fig. 9. SEM micrographs of the 10% Cr steel in the gauge section of specimens after creep tests at 650 °C under a stress of 120 MPa: (a) specimen A (1000 h); (b) specimen B (10000 h); (c) specimen C (28286 h); (d) ruptured specimen (39437 h). Change in the particle density at (sub)grain boundaries (e) and the mean size of precipitates (f) with time estimated by SEM. Densities of $M_{23}C_6$ and Laves phase particles at (sub)grain boundaries were calculated by technique from [19].

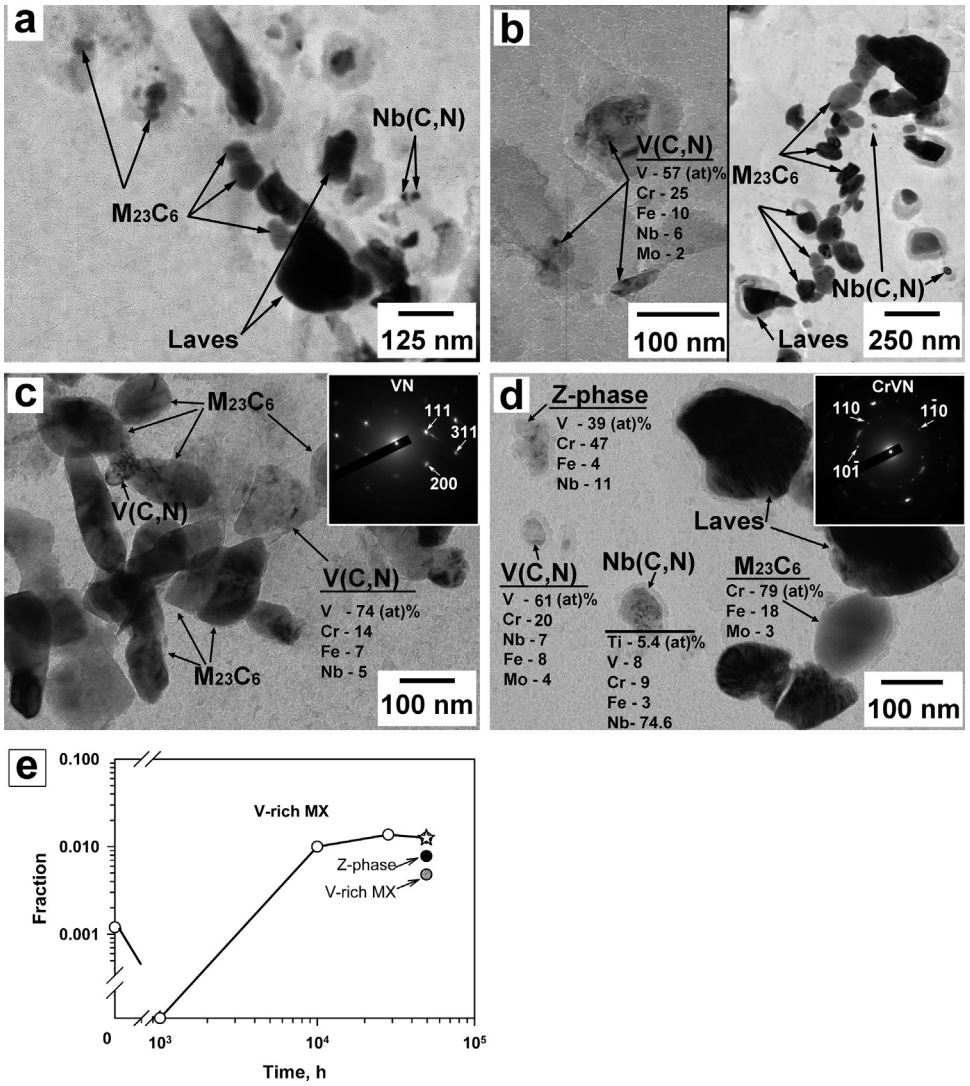

Fig. 10. TEM micrographs of the 10% Cr steel show precipitates after creep tests at 650 °C under a stress of 120 MPa: a) specimen A (1000 h), gauge portion; (b) specimen B (10000 h), gauge portion; (c) ruptured specimen (39437 h), grip portion; and (d) ruptured specimen (39437 h), gauge portion. Change in the fraction of V-rich M(C,N) particles estimated on replicas by TEM with time in the gauge portion (e).

grip section after ~$4{\cdot}10^4$ h of long-term aging are nearly equivalent (Table 1). Therefore, creep accelerates the precipitation and coarsening of V-rich M(C,N) carbonitrides by a factor of ~4. Rough estimation of the fraction of V-rich particles on replicas by TEM showed that steady-state creep leads to an approximate 10-fold increase relative to that after transient creep (Fig. 10(e)). Further creep insignificantly affects their volume fraction and dimensions (Fig. 10(e), Table 1).

Strain-induced growth of Laves phase particles was evident (Table 1, Figs. 5(c), 8(b) and 9(b)). It is worth noting that coarsening of the Laves phase particles was not accompanied by dissolution of the precipitates that were located at the interlath boundaries. Coarse Laves phase particles were observed at both the interlath and PAG boundaries. Moreover, new Laves phase particles with an average size of ~170 nm precipitate on the interlath boundaries during steady-state creep. This process also occurs during tertiary creep, which increases the volume fraction of Laves phase particles with strain.

Distinct strain-induced coarsening of $M_{23}C_6$ carbides occurs under tertiary creep (Table 1, Figs. 8(c) and (d), 9(c) and (d), 10(d)). After the first stage of tertiary creep, chains of fine $M_{23}C_6$ carbides and coarse Laves phase particles remain at the majority of the interlath boundaries; after the secondary stage of tertiary creep, these chains are only observed at some of the interlath boundaries. It is worth noting that these $M_{23}C_6$ carbides exhibit superior coarsening resistance during creep than other 9–11% Cr steels containing 0.1 wt% C and 0.05 wt% N [11,19,21–23,35,50]. The mean size of the carbides increases by only 70% after ~$4{\cdot}10^4$ h of creep. Both long-term aging and creep affect the chemical composition of the $M_{23}C_6$ carbides: the Cr content increases from ~67 to ~78 at% and the Fe content decreases from ~28 to ~17 at%. The contents of the other elements (V and Mo) remain essentially unchanged. No enrichment of the $M_{23}C_6$ carbides by V [51] was evident even after ~$4{\cdot}10^4$ h of aging and creep.

The formation of several Z-phase particles (CrVN) with a mean size of 120 nm was evident in the ruptured specimen (Fig. 10(d)). As only V-rich M(C,N) precipitates were observed in the grip portion of this specimen (Fig. 10(c)), this transformation is strain-induced. Z-phase particles are more enriched by Cr (up to 40–50 at%) in the metallic matrix than V-rich M(C,N) particles, which is in agreement with the identification criterion for the Z-phase [17,18]. However, the strain-induced formation of a Z-phase could not affect the creep strength of the 10% Cr steel because of the negligible number and small sizes of the Z-phase particles. In general, a dispersion of M(C,N) remains after ~$4{\cdot}10^4$ h of creep. Moreover, the volume fraction of these carbonitrides significantly increases because of the additional precipitation of V-rich dispersoids. During creep, the number of Nb-rich M(C,N) carbonitrides enriched by Ti (4–7% at.) tends to increase with strain.

4. Discussion

4.1. Correlation between creep behavior and microstructural changes

The main characteristic of microstructural evolution in the present steel during long-term creep at 650 °C and 120 MPa is the retention of the lath structure up to rupture. An increase in the lath thickness and a decrease in the dislocation density occurred gradually in the transient and apparent steady-state stages (Fig. 5(a,b)). In contrast, drastic changes in the lath structure occurred in the tertiary creep that were caused by the coarsening of Laves phase particles (Figs. 5(a–c), 9(f)) and corresponding depletion of the solid solution by substitutional elements of W and Mo (Fig. 3). Nevertheless, TMLS did not transform into the subgrain structure. Moreover, the gradual evolution of TMLS during the transient and steady-state creep was not accompanied by a remarkable release of internal stresses. The KAM distribution in Fig. 6 suggests that large lattice distortions remained in the specimen until the second stage of tertiary creep. It is obvious that the 10% Cr steel with low N and high B content exhibits specific precipitation behavior during long-term creep, which suppresses or shifts the creep strength breakdown to higher rupture times.

In the previous study [12], the analysis of short-term creep behavior (with creep rupture time of 1426 h) of the 10%Cr steel under an applied stress of 140 MPa showed that no significant changes occurred in TMLS under creep conditions up to rupture. So, an increase in the creep rate in the tertiary stage and the creep fracture occurred due to a contribution of factors determined by a high level of applied stress such as necking, cavitation, and localization of deformation near the PAG boundaries [9]. The value of parameter $d \ln \dot{\varepsilon}/d\varepsilon < 100$ in the tertiary stage (Fig. 2(c)) confirms this finding [9,12]. According to Abe [9], the parameter $d \ln \dot{\varepsilon}/d\varepsilon$ above 100 in the tertiary stage is indicative of the contribution of microstructure in the creep resistance. Therefore, the long-term creep resistance of the 10%Cr steel is affected by the microstructural factors, in contrast to short-term creep behavior [12].

The transient stage was characterized by the absolute value of $d \ln \dot{\varepsilon}/d\varepsilon (\sim 576)$ (Fig. 2(c)), which was ~4 times higher than that at 140 MPa (~145) [12]; this was attributed to an increase in the $d\dot{\varepsilon}$ value by a factor of ~100. Therefore, the transition from short- to long-term conditions results in a decreased $\dot{\varepsilon}_{min}$ value. It is obvious that this is the main reason for the lack of creep strength breakdown. The dramatic decrease in the $\dot{\varepsilon}_{min}$ value upon decreasing the applied stress from 140 to 120 MPa was a surprising result (Table 2), because this value at 120 MPa was about an order of magnitude lower as compared to that for 3%Co-modified P92 steel [11], whereas at 140 MPa both steels demonstrated nearly the same minimum creep rate [11,12].

Also, the rate of acceleration of the tertiary creep, p, was approximately 2 orders of magnitude lower than that during short-term creep at 140 MPa (Table 2). This is an evidence for significant slow down recovery processes in the tertiary creep. Therefore, creep resistance is strongly affected by the tertiary creep behavior and, especially, at the first stage of tertiary creep.

So, the high stability of the lath structure and precipitates in the steady-state stage and the first stage of tertiary creep plays a vital role in the long-term creep resistance of the 10%Cr steel.

Under creep conditions, the TMLS could be stabilized by three factors: (i) substitutional alloying element within the ferritic matrix; (ii) a dispersion of fine boundary $M_{23}C_6$ carbides and Laves phase particles; (iii) a dispersion of M(C,N) carbonitrides, which are homogeneously distributed in the ferritic matrix. The boundary particles exert a large Zener drag force which effectively hinders migration of low- and high-angle boundaries [11]. M(C,N) carbonitrides located in ferritic matrix and such substitutional solutes as W and Mo hinder the rearrangement of lattice dislocations that suppresses the knitting reaction between lattice dislocations and lath boundaries. The last prevents the transformation of lath boundaries, which are in fact irregular dislocation arrays, to subboundaries.

Let us consider effect of these strengthening factors on the long-term creep behavior of the 10%Cr steel.

4.2. Solid solution strengthening

The gradual depletion of W and Mo from the solid solution correlated with the microhardness decrease in the grip section of the creep tested specimens (Fig. 3), i.e. the solid- solution strengthening continuously decreased with time due to the W and Mo depletion and formation of Laves phase. Due to the fact that the microhardness decrease was more pronounced in the gauge section of specimen than in grip one, it was associated not only with the solid-solution softening but also with the strain-induced softening due to the changes in TMLS such as the martensite lath widening and decrease in the lattice dislocation density.

The depletion of W from the solid solution obviously provoked the acceleration of the knitting reaction, which in turn, resulted in the significant changes in TMLS. Thus, the depletion of W from the solid solution in the tertiary creep stage correlated with the acceleration of the lath widening and decrease in the dislocation density and acceleration of the coarsening of Laves phase particles and $M_{23}C_6$ carbides. Although the W and Mo depletion and corresponding solid-solution softening occurred during creep, the lath structure did not transform into a subgrain structure. It can be concluded that the absence of this agent associated with the W and Mo alloying elements within the ferritic matrix cannot provoke the degradation of TMLS and creep resistance of the 10%Cr steel. Nevertheless, the depletion of the solid solution can cause the transition from the first to second stage in tertiary creep.

4.3. Dispersion of boundary $M_{23}C_6$ carbides and Laves phase particles

Although the depletion of W from the solid solution in the tertiary creep stage correlated with an acceleration of coarsening of both Laves phase particles and $M_{23}C_6$ carbides, only the Laves phase particle coarsening could be considered as a reason for TMLS changes, because the dimensions of $M_{23}C_6$ carbides remained on the nanoscale level (mean size was 120 nm) (Fig. 5(c)) and they were densely distributed along the boundaries up to rupture (Fig. 8).

Simulation of the coarsening kinetics of the $M_{23}C_6$ and Laves phase particles at 650 °C for model compositions of the 10% Cr steel (Fig. 11(a)) revealed that the experimental coarsening rate of the $M_{23}C_6$ particles matches that of the theoretical calculations based on an interfacial energy of 0.01 J/m^2. This value is a 10-fold lower than that estimated for the short-term (up to 2000 h) creep [12].

It is worth noting that the coarsening kinetics of $M_{23}C_6$ carbides in a 9 wt% Cr – 2 wt% W – 3 wt% Co steel are best described by theoretical calculations based on an interfacial energy of 0.36 J/m^2 [35]. Therefore, the main difference between high Cr steel with 0.1 wt% C and 0.05 wt% N and high B steel is the coherency of the interfaces of these carbides. Coherent or semi-coherent interfaces of $M_{23}C_6$ particles with a lowest misfit value $[(011)_\alpha||(111)_{M23C6}]$ of 1.1% are associated with either the Kurdjumov-Sachs (KS) [52] orientation relationship,

$$\left((011)_\alpha||(111)_{M_{23}C_6}[\bar{1}1\bar{1}]_\alpha||[01\bar{1}]_{M_{23}C_6}\right), \quad (3)$$

or the Nishiyama-Wasserman (NW) orientation relationship [52,53],

$$\left((011)_\alpha||(111)_{M_{23}C_6}[100]_\alpha||[01\bar{1}]_{M_{23}C_6}\right). \quad (4)$$

However, the NW orientation relationship provides a high misfit value $[(100)_\alpha||(110)_{M23C6}]$ of 12.4% [52]. Three other orientation relationships, which were experimentally found in a 10% Cr steel with 0.1 wt% C and 0.05 wt% N, provide higher misfit values [54]. The KS orientation relationship of the $M_{23}C_6$ carbides in the present 10% Cr steel is retained under short-term creep conditions until rupture [12]. Fig. 12 shows that the $M_{23}C_6$ carbides located on the interlath

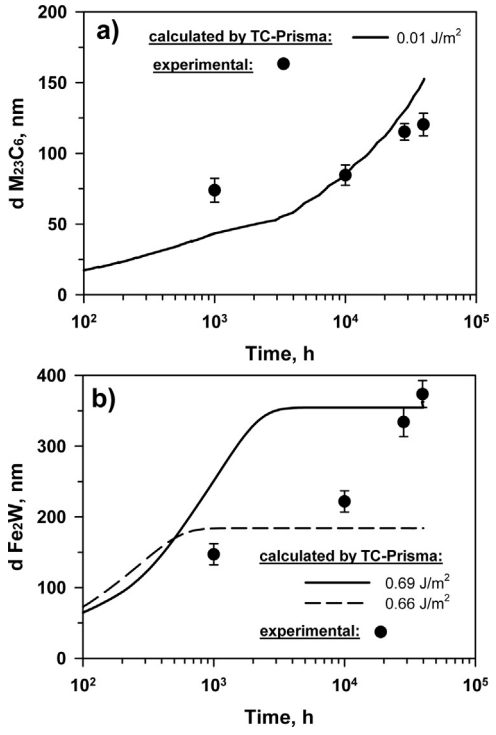

Fig. 11. Calculated and experimental results on coarsening of $M_{23}C_6$ (a) and Laves phase (b) particles at 650 °C in the 10%Cr steel. Lines indicate the calculated temporal dependence of size of particles in the model composition (0.1C-10Cr-3.1Co-0.7Mo-2.0W-Fe). Symbols indicate the experimental results on the mean size of particles during creep testing at 650 °C under a stress of 120 MPa.

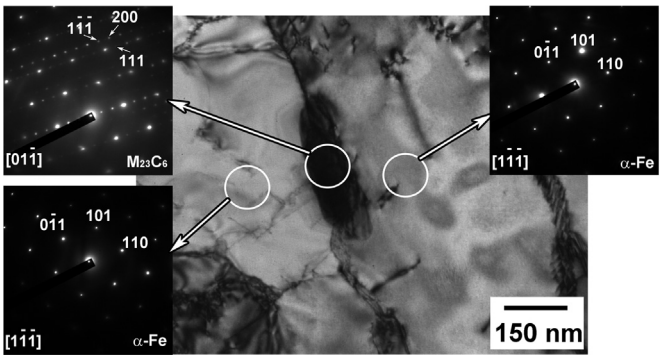

Fig. 12. Microstructure and SAD patterns from the $M_{23}C_6$ carbide and ferritic matrix of the 10% Cr steel creep ruptured at 650 °C under a stress of 120 MPa.

boundaries also exhibit the KS orientation relationship after rupture. Therefore, these carbides retain the coherency of their interfaces under long-term creep despite the rupture time increasing from $\sim 1.5{\cdot}10^3$ to $\sim 4{\cdot}10^4$ h. Strain may lead to the loss of coherency or a transition from coherent to semi-coherent interfaces that is accompanied by a significant increase in the energy of the interfaces and, therefore, highly accelerated Ostwald ripening [35,36]. However, the majority of the $M_{23}C_6$ particles retain the coherency of their interfaces. As a result, chains of these carbides on the interlath boundaries are also retained during long-term creep, thereby preventing the formation of a distinct subgrain structure.

Coarsening of the Laves phase particles occurs at a high rate. The coarsening behavior of these particles can be described by theoretical calculations based on an interfacial energy of 0.66 J/m^2 up to 10^4 h and 0.69 J/m^2 from 10^4 to $4{\cdot}10^4$ h (Fig. 11(b)). It is worth noting that these values are approximately the same as that estimated for short-term creep [12]. The difference in the interfacial energies at apparent steady-state and tertiary creep was attributed to the Ostwald ripening of the Laves phase particles during tertiary creep [35,36].

4.4. Dispersion of homogeneously distributed M(C,N) carbonitrides

During the transient creep stage, M(C,N) carbonitrides were presented mainly by Nb-rich carbonitrides, whereas scarce V-rich M(C,N) particles, precipitated during tempering, were not revealed after 1000 h of creep and aging conditions (Figs. 5(d), 10), that was correlated with the same observation after short-term creep at 140 MPa [12]. Nb-rich carbonitrides were highly stable up to rupture. Probably, enrichment of Nb-rich M(C,N) particles by Ti (Fig. 10(d)), that started to occur at the transient stage, additionally increased their coarsening resistance.

The minimum creep rate stage was accompanied by the precipitation of V-rich M(C,N) carbonitrides, which along with Nb-rich carbonitrides effectively pinned the lattice dislocations in the lath interiors. TEM observations revealed numerous dislocations arrested by fine particles in the lath interiors after 10000 h of creep. The precipitation of V-rich M(C,N) particles is in agreement with Thermo-Calc calculations that predict their several times higher equilibrium fraction at 650 °C than that at 770 °C, corresponding to tempering temperature. As the TEM analysis showed lattice dislocations attached to almost all the carbonitrides, we can presume that V-rich M(C,N) carbonitrides precipitate onto dislocations to render them immobile. It is well-known that Nb-rich M(C,N) particles enriched with C precipitate on dislocations while V-rich M(C,N) particles enriched with N precipitate homogeneously during tempering [37,38,40]. Accordingly, precipitation of V-rich M(C,N) carbonitrides onto dislocations can be attributed to their enrichment with C. These particles precipitate very slowly. It is apparent that the negligible amount of V-rich M(C,N) carbonitrides that precipitate during tempering in low N 9–10% Cr steels [34,38] were enriched with N as their shapes and dimensions are different from those that precipitate during long-term aging or creep. It is known [1,2] that a dispersion of M(C,N) carbonitrides plays a key role in the superior creep resistance of new generation 9–11% Cr steels. The low volume fraction of V-rich M(C,N) carbonitrides that precipitate during tempering does not impart any advantages to high B and low N 10% Cr steel relative to steels with the same contents of substitutional solutes under short-term creep conditions [11,12,21–23,27,28,54]. In contrast, under long-term creep, additionally precipitated V-rich M(C,N) carbonitrides effectively impede gliding dislocations.

During the second stage of tertiary creep (between 28286 and 39347 h), a part of V-rich M(C,N) particles started to transform into Z-phase. However, the Z-phase did not degrade the creep strength remarkably because of quite small size of the Z-phase particles that were almost the same as preceding M(C,N) particles.

4.5. Evolution of pinning pressures during creep

Analysis of the pinning of (sub)grain/interlath boundaries by various secondary-phase particles allows us to estimate the role of different precipitates in the stabilization of the TMLS under creep conditions. The pinning pressures exerted by different precipitates on the grain/subgrain boundaries were estimated using a technique described in [11,12,19,21–23]. Homogeneously distributed M(C,N) carbonitrides exert Zener pinning pressure on a boundary, which can be estimated as follows [11,19,21–23,26]:

$$P_Z = \frac{3\gamma F_V}{d} \tag{5}$$

where γ is the boundary surface energy per unit area, and F_v and d are the volume fraction and size of dispersed particles, respectively. The pinning pressure exerted by boundary particles depends on the ratio of dimensions between these particles and subgrains/laths [11,19,21,23,55], and can be evaluated as follows:

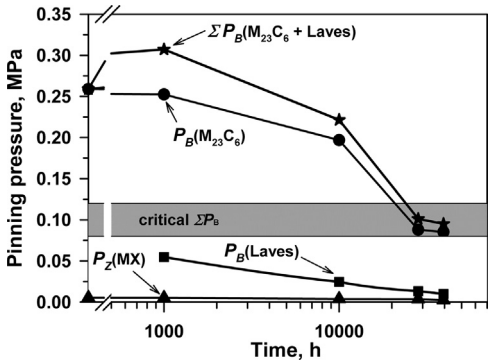

Fig. 13. Change in the pinning pressures from different particles on the (sub)grain and lath boundaries in the gauge section of the 10% Cr steel during creep testing at 650 °C under a stress of 120 MPa.

$$P_B = \frac{\gamma F_{vB} D}{d^2} \quad (6)$$

where F_{vB} is the volume fraction of the particles located at the boundaries, and D is the size of structural elements, i.e. the subgrain size or lath thickness. Technique for calculation of F_{vB} value was reported in [11,12,19,22]. The densities of boundary $M_{23}C_6$ and Laves phase particles were calculated under the assumption that all $M_{23}C_6$ and Laves phase particles located at interlath and (sub)grain boundaries (Fig. 9(e)).

Fig. 13 shows the effect of creep on the pinning pressures. It is clear that the pinning pressure exerted from the boundary $M_{23}C_6$ carbides is extremely high and the Zener drag exerted by the M(C,N) carbonitrides is negligible because of the low fraction of M(C,N) carbonitrides. The Laves phase particles precipitate during transient creep and exert a pinning pressure that is smaller by a factor ranging from 3 to 8 than that exerted by $M_{23}C_6$ carbides. At the onset of apparent steady-state creep, the pinning pressure exerted by $M_{23}C_6$ carbides remains almost unchanged (approximately 0.25 MPa) while that exerted by the Laves phase particles tends to decrease with strain. Under tertiary creep, the pinning pressure from the $M_{23}C_6$ carbides decreases significantly. The total pinning pressure exerted by both the $M_{23}C_6$ carbides and Laves phase particles drops below the critical value of 0.12 MPa [11] after termination of the first stage of tertiary creep. As was shown previously [11], the transformation of the TMLS to a subgrain structure occurs if the Zener drag force is less than the critical value that leads to creep strength breakdown. In the 10% Cr steel, this drop accelerates the kinetics process during tertiary creep. However, the Zener drag force exerted by the $M_{23}C_6$ particles remains high ($\geq$0.08 MPa). In addition, discontinuous chains of $M_{23}C_6$ carbides were observed at the interlath boundaries because the coarsening process does not lead to dissolution of these precipitates. As a result, only some of the interlath boundaries can detach from these chains. The decrease of the Zener drag force below the critical value leads to a transition from slow acceleration during the first stage to rapid acceleration during the second stage of tertiary creep because of accelerated lath coarsening and decreased lattice dislocation density. However, a well-defined subgrain structure does not form until rupture and no creep strength breakdown appears.

Thus, $M_{23}C_6$ carbides are the most effective pinning agent in 10% Cr steel with high B and low N contents. Under transient and steady-state creep, these particles impede the knitting reaction by pinning dislocations, and, under tertiary creep, they hinder lath coarsening, which prevents the transformation of the TMLS to equiaxed grains.

4.6. Reasons for superior creep resistance

The Σ(W + Mo) content reaching the thermodynamic equilibrium content in the ferritic matrix during the tertiary creep stage correlates with the onset of strain-induced coarsening of both types of boundary particles ($M_{23}C_6$ carbides and Laves phase particles), which is a characteristic feature of long-term creep [11,21]. However, the rate of the kinetic reaction during the first stage of tertiary creep is low, which was attributed to the high coarsening resistance of interlath $M_{23}C_6$-type carbides and M(C,N) carbonitrides located in the ferritic matrix. The knitting reaction occurs at a high rate if all three agents partially or completely lose their ability to pin gliding dislocations. In 10% Cr steel, the boundary $M_{23}C_6$ particles and M(C,N) carbonitrides hinder the knitting reaction until rupture. The knitting reaction is complete upon the onset of the secondary stage of tertiary creep, which is characterized by accelerated lath coarsening and a high proportion of strain-free areas within the PAGs (Fig. 6(h)).

V-rich M(C,N) carbonitrides that nucleate on dislocations effectively impede gliding dislocations, which compensates for the coarsening of the boundary particles and depletion of W and Mo solutes from the ferritic matrix. Therefore, the depletion of W atoms, which are effective point-like obstacles to the motion of dislocations and highly decrease diffusivity, is not necessary for the appearance of creep strength breakdown in the 10% Cr steel with high B and low N; this is in contrast to the behavior of 9% Cr steel [11]. The dispersion of nanoscale boundary $M_{23}C_6$ carbides and Laves phase particles and increased volume fraction of M(C,N) carbonitrides suppresses the knitting reaction even at low solid-solution contents of W. The internal stress field is only relieved in the vicinity of the PAG boundaries. It is evident that superposition of these three factors significantly decreases the rate of the knitting reaction. Although it is impossible to completely suppress the knitting reaction, bringing the applied stress close to the threshold stress value and introducing effective pinning agents in the ferritic matrix and on the interlath boundaries impedes this kinetic reaction. The remarkable transformation of the lath boundaries, which are actually irregular dislocation arrays, to subboundaries occurs only during tertiary creep after a duration $\geq 10^4$ h because of the low rate of the knitting reaction; this is provided by the formation of continuous chains of boundary particles at the interlath boundaries during transient creep and precipitation of V-rich non-shearable carbonitrides during steady-state creep. As a result, the creep strength of these 9–10% Cr steels increases leading to the creep rupture time at 650 °C being ~10 times larger than that of high Cr steels with 0.1 wt% C and 0.05 wt% N [5,6,11,12,21–23,27,28,31,32,54]. The later ones exhibit similar level of the creep rupture time at remarkably lower temperature of 600 °C.

5. Conclusions

The creep behavior and evolution of lath structure and precipitates during at 650 °C under an applied stress of 120 MPa for the 10% Cr steel with 3% Co, 0.008% B, and 0.003% N were studied and the following conclusions can be drawn:

1. The steel demonstrates superior creep resistance with a time-to-rupture of 39 437 h and a minimum creep rate of $1.15 \cdot 10^{-7}$ h^{-1}. The steel exhibits two-stage tertiary creep behavior. The transition from the first stage of the slow acceleration of the creep rate with a $d \ln \dot{\varepsilon}/d\varepsilon$ value of ~139 to the second stage of rapid acceleration of the creep rate with a $d \ln \dot{\varepsilon}/d\varepsilon$ value of ~354 occurs at ~$2.8 \cdot 10^4$ h.
2. The tempered martensite lath structure of the 10% Cr steel remains stable during long-term creep testing until rupture. The evolution of the lath structure is nearly the same under a transient, apparent steady-state, and appropriate long-term aging. Strong strain-induced lath coarsening appears during tertiary creep. The lattice dislocation density significantly decreases during transient and tertiary creep.
3. During long-term aging, the Laves phase particles precipitate at the interlath boundaries and high-angle boundaries of the blocks, packets, PAGs, and V-rich M(C,N) carbonitrides within the ferritic matrix followed by their extensive coarsening. The $M_{23}C_6$ carbides are resistant to static coarsening.
4. During transient creep, the Laves phase particles precipitate in the

same manner as that during long-term aging. During apparent steady-state creep, the V-rich M(C,N) carbonitrides precipitate within the ferritic matrix. Strain-induced coarsening of the $M_{23}C_6$ carbides and Laves phase particles occurs during tertiary creep.

5. Nanoscale $M_{23}C_6$ carbides and M(C,N) carbonitrides can compensate for the negative effects of W depletion from the solid solution and extensive coarsening of the Laves phase particles; this results in superior long-term creep resistance.
6. The superior coarsening resistance of the $M_{23}C_6$ carbides is attributed to the low interfacial energy (0.01 J/m^2) of their coherent interfaces. The majority of $M_{23}C_6$ carbides retain their Kurdjumov-Sachs orientation relationship with the ferritic matrix until rupture. $M_{23}C_6$ carbides exert high pinning pressure ($\geq$0.08 MPa).
7. Strain-induced formation of Z-phase does not affect the creep strength under applied stress of 120 MPa due to nanoscale size of Z-phase particles.

Acknowledgments

The study was financial supported by the Ministry of Education and Science of Russian Federation, under project of Government Task No. 11.2868.2017/PCh. The authors are grateful to the staff of the Joint Research Center, Belgorod State University, for providing the equipment for instrumental analysis.

References

[1] F. Abe, T.-U. Kern, R. Viswanathan, Creep-Resistant Steels, Woodhead Publishing, Cambridge, 2008.
[2] R.O. Kaybyshev, V.N. Skorobogatykh, I.A. Shchenkova, New martensitic steels for fossil power plant: creep resistance, Phys. Metal. Metallogr. 109 (2010) 186–200.
[3] A. Kostka, K.-G. Tak, R.J. Hellmig, Y. Estrin, G. Eggeler, On the contribution of carbides and micrograin boundaries to the creep strength of tempered martensite ferritic steels, Acta Mater. 55 (2007) 539–550.
[4] A. Aghajani, Ch Somsen, G. Eggeler, On the effect of long-term creep on the microstructure of a 12% chromium tempered martensite ferritic steel, Acta Mater. 57 (2009) 5093–5106.
[5] K. Kimura, H. Kushima, K. Sawada, Long-term creep deformation property of modified 9Cr–1Mo steel, Mater. Sci. Eng. A 510–511 (2009) 58–63.
[6] M. Yoshizawa, M. Igarashi, K. Moriguchi, A. Iseda, H.G. Armaki, K. Maruyama, Effect of precipitates on long-term creep deformation properties of P92 and P122 type advanced ferritic steels for USC power plants, Mater. Sci. Eng. A 510–511 (2009) 162–168.
[7] H.G. Armaki, R. Chen, K. Maruyama, M. Igarashi, Creep behavior and degradation of subgrain structures pinned by nanoscale precipitates in strength- enhanced 5 to 12 pct Cr ferritic steels, Metall. Mater. Trans. A 42 (2011) 3084–3094.
[8] H.G. Armaki, R. Chen, K. Maruyama, M. Igarashi, Contribution of recovery mechanisms of microstructure during long-term creep of Gr.91steels, J. Nucl. Mater. 433 (2013) 23–29.
[9] F. Abe, Creep behavior, deformation mechanisms and creep life of mod.9Cr-1Mo steel, Metall. Mater. Trans. A 46 (2015) 5610–5625.
[10] V.A. Dudko, A.N. Belyakov, R.O. Kaibyshev, Sources of high creep resistance of modern high-chromium martensitic steels, Dokl. Phys. Chem. 464 (2015) 191–193.
[11] A. Fedoseeva, N. Dudova, R. Kaibyshev, Creep strength breakdown and microstructure evolution in a 3%Co modified P92 steel, Mater. Sci. Eng. A 654 (2016) 1–12.
[12] R. Mishnev, N. Dudova, R. Kaibyshev, Microstructural aspects of superior creep resistance of a 10%Cr martensitic steel, Mater. Sci. Eng. A 678 (2016) 178–189.
[13] V. Dudko, A. Belykov, R. Kaibyshev, Evolution of lath substructure and internal stresses in a 9% Cr steel during creep, ISIJ Int. 57 (2017) 540–549.
[14] M. Mitsuhara, Sh Yamasaki, M. Miake, H. Nakashima, M. Nishida, J. Kusumoto, A. Kanaya, Creep strengthening by lath boundaries in 9Cr ferritic heat resistant steel, Philos. Mag. Lett. 96 (2016) 76–83.
[15] L. Morsdorf, O. Jeannin, D. Barbier, M. Mitsuhara, D. Raabe, C.C. Tasan, Multiple mechanisms of lath martensite plasticity, Acta Mater. 121 (2016) 202–214.
[16] W. Bendick, L. Cipolla, J. Gabrel, J. Hald, New ECCC assessment of creep rupture strength for steel grade X10CrMoVNb9-1 (Grade 91), Int. J. Press. Vessel. Pip. 87 (2010) 304–309.
[17] L. Cipolla, H.K. Danielsen, D. Venditti, P.E. Di Nunzio, J. Hald, M.A.J. Somers, Conversion of MX nitrides to Z-phase in a martensitic 12%Cr steel, Acta Mater. 58 (2010) 669–679.
[18] H.K. Danielsen, Review of Z phase precipitation in 9–12 wt%Cr steels, Mater. Sci. Technol. 32 (2016) 126–137.
[19] N. Dudova, A. Plotnikova, D. Molodov, A. Belyakov, R. Kaibyshev, Structural changes of tempered martensitic 9%Cr–2%W–3%Co steel during creep at 650 °C, Mater. Sci. Eng. A 534 (2012) 632–639.
[20] L. Helis, Y. Toda, T. Hara, H. Miyazaki, F. Abe, Effect of cobalt on the microstructure of tempered martensitic 9Cr steel for ultra-supercritical power plants, Mater. Sci. Eng. A 510–511 (2009) 88–94.
[21] A. Fedoseeva, N. Dudova, R. Kaibyshev, Creep behavior and microstructure of a 9Cr–3Co–3W martensitic steel, J. Mater. Sci. 52 (2017) 2974–2988.
[22] V. Dudko, A. Belyakov, D. Molodov, R. Kaibyshev, Microstructure evolution and pinning of boundaries by precipitates in a 9pctCr heat resistant steel during creep, Metall. Mater. Trans. A 44 (2013) 162–172.
[23] A. Kipelova, R. Kaibyshev, A. Belyakov, D. Molodov, Microstructure evolution in a 3%Co modified P911 heat resistant steel under tempering and creep conditions, Mater. Sci. Eng. A 528 (2011) 1280–1286.
[24] R. Kaibyshev, R. Mishnev, A. Fedoseeva, N. Dudova, The role of microstructure in creep strength of 9-12%Cr steels, Mater. Sci. Forum 879 (2017) 36–41.
[25] F. Abe, Analysis of creep rates of tempered martensitic 9%Cr steel based on microstructure evolution, Mater. Sci. Eng. A 510–511 (2009) 64–69.
[26] F.J. Humphreys, M. Hatherly, Recrystallization, Related Annealing Phenomena, second ed, Elsevier, Oxford, 2004.
[27] H. Semba, F. Abe, Alloy design and creep strength of advanced 9%Cr USC boiler steels containing high concentration of boron, Energy Mater. 1 (2006) 238–244.
[28] M. Tabuchi, H. Hongo, F. Abe, Creep strength of dissimilar welded joints using high B-9Cr steel for advanced USC boiler, Metall. Mater. Trans. A 45 (2014) 5068–5075.
[29] R. Kaibyshev, R. Mishnev, E. Tkachev, N. Dudova, Effect of Ni and Mn on the creep behavior of 9-10%Cr steels with low N and high B, Trans. Indian Inst. Met. 69 (2016) 203–210.
[30] Y. Liu, S. Tsukamoto, K. Sawada, M. Tabuchi, F. Abe, Precipitation behaviour in Ac3 HAZ simulated B steel during PWHT and creep deformation, Metall. Mater. Trans. A 46 (2015) 1843–1854.
[31] F. Abe, Effect of boron on microstructure and creep strength of advanced ferritic power plant steels, Procedia Eng. 10 (2011) 94–99.
[32] F. Abe, Research and development of heat-resistant materials for advanced USC power plants with steam temperatures of 700 °C and above, Engineering 1 (2015) 211–224.
[33] R. Sahara, T. Matsunaga, H. Hongo, M. Tabuchi, Theoretical investigation of stabilizing mechanism by boron in body-centered cubic iron through $(Fe,Cr)_{23}(C,B)_6$ precipitates, Metall. Mater. Trans. A 47 (2016) 1–11.
[34] N. Dudova, R. Kaibyshev, On the precipitation sequence in a 10%Cr Steel under tempering, ISIJ Int. 51 (2011) 826–831.
[35] A. Fedoseeva, E. Tkachev, V. Dudko, N. Dudova, R. Kaibyshev, Effect of alloying on interfacial energy of precipitation/matrix in high-chromium martensitic steels, J. Mater. Sci. 52 (2017) 4197–4209.
[36] D.A. Porter, K.E. Esterling, M. Sherif, Phase Transformation in Metals and Alloys, third, CRS Press, Boca Raton, Florida, 2009.
[37] N. Dudova, R. Mishnev, R. Kaibyshev, Effect of tempering on microstructure and mechanical properties of boron containing 10%Cr steel, ISIJ Int. 51 (2011) 1912–1918.
[38] I. Fedorova, A. Kostka, E. Tkachev, A. Belyakov, R. Kaibyshev, Tempering behavior of a low nitrogen boron-added 9%Cr steel, Mater. Sci. Eng. A 662 (2016) 443–455.
[39] A. Fedoseeva, N. Dudova, U. Glatzel, R. Kaibyshev, Effect of W on tempering behaviour of a 3%Co modified P92 steel, J. Mater. Sci. 51 (2016) 9424–9439.
[40] N. Saeidi, F. Ashrafizadeh, B. Niroumand, F. Barlat, EBSD study of damage mechanisms in a high-strength ferrite-martensite dual-phase steel, J. Mat. Eng. Perform. 24 (1) (2015) 53–58.
[41] R. Mishnev, N. Dudova, R. Kaibyshev, Low cycle fatigue behavior of a 10% Cr martensitic steel at 600 °C, ISIJ Int. 55 (2015) 2469–2476.
[42] H. Kitahara, R. Ueji, N. Tsuji, Y. Minamino, Crystallographic features of lath martensite in low-carbon steel, Acta Mater. 54 (2006) 1279–1288.
[43] I. Zuiko, R. Kaibyshev, Deformation structures and strengthening mechanisms in an Al-Cu alloy subjected to extensive cold rolling, Mater. Sci. Eng. A 702 (2017) 53–64.
[44] F. Garofalo, Fundamentals of Creep and Creep Rupture in Metals, MacMillan, New York, NY, 1965.
[45] J. Vanaja, K. Laha, M.D. Mathew, Effect of tungsten on primary creep deformation and minimum creep rate of reduced activation ferritic-martensitic steel, Metall. Mater. Trans. A 45 (2014) 5076–5084.
[46] J. Vanaja, K. Laha, Assessment of tungsten content on tertiary creep deformation behavior of reduced activation ferritic-martensitic steel, Metall. Mater. Trans. A 46 (2015) 4669–4679.
[47] R.K. Ray, J.J. Jonas, Transformation textures in steels, Int. Mater. Rev. 35 (1) (1990) 1–36.
[48] A. Kipelova, A. Belyakov, R. Kaibyshev, Laves phase evolution in a modified P911 heat resistant steel during creep at 923 K, Mater. Sci. Eng. A 532 (2012) 71–77.
[49] I. Fedorova, A. Belyakov, P. Kozlov, V. Skorobogatykh, I. Shenkova, R. Kaibyshev, Laves-phase precipitates in a low-carbon 9% Cr martensitic steel during aging and creep at 923 K, Mater. Sci. Eng. A 615 (2014) 153–163.
[50] A. Kipelova, M. Odnobokova, A. Belyakov, R. Kaibyshev, Effect of Co on Creep Behavior of a P911 Steel, Metall. Mater. Trans. A 44 (2013) 577–583.
[51] Y. Xu, X. Zhang, Y. Tian, C. Chen, Y. Nan, H. He, M. Wang, Study on the nucleation and growth of M23C6 carbides in a 10% Cr martensite ferritic steel after long-term aging, Mater. Charact. 111 (2016) 122–127.
[52] A. Kipelova, A. Belyakov, R. Kaibyshev, The crystallography of $M_{23}C_6$ carbides in martensitic 9% Cr steel after tempering, aging and creep, Philos. Mag. 93 (2013) 2259–2268.
[53] K.H. Kuo, C.L. Jia, Crystallography of $M_{23}C_6$ and M_6C precipitated in a low alloy steel, Acta Metall. 33 (1985) 991–996.
[54] Y. Liu, S. Tsukamoto, K. Sawada, F. Abe, Role of boundary strengthening on prevention of type IV failure in high Cr ferritic heat-resistant steels, Metall. Mater. Trans. A 45 (3) (2014) 1306–1314.
[55] W.B. Hutchinson, B.J. Duggan, Influence of precipitation on recrystallization and texture development in an iron-1.2% copper alloy, Met. Sci. 12 (1978) 372–380.